Physics of Fluids

The impact of hemodynamic factors in a coronary main artery to detect the atherosclerotic severity: Single and multiple sequential stenosis cases

Cite as: Phys. Fluids **33**, 031903 (2021); https://doi.org/10.1063/5.0041335
Submitted: 25 December 2020 . Accepted: 02 February 2021 . Published Online: 04 March 2021

K. E. Hoque, M. Ferdows, S. Sawall, E. E. Tzirtzilakis, and M. A. Xenos

Physics of Fluids ARTICLE scitation.org/journal/phf

The impact of hemodynamic factors in a coronary main artery to detect the atherosclerotic severity: Single and multiple sequential stenosis cases

Cite as: Phys. Fluids **33**, 031903 (2021); doi: 10.1063/5.0041335
Submitted: 25 December 2020 · Accepted: 2 February 2021 ·
Published Online: 4 March 2021

View Online Export Citation CrossMark

K. E. Hoque,[1,2] M. Ferdows,[1,a)] S. Sawall,[3] E. E. Tzirtzilakis,[4] and M. A. Xenos[5]

AFFILIATIONS

[1]Research Group of Fluid Flow Modeling and Simulation, Department of Applied Mathematics, University of Dhaka, Dhaka-1000, Bangladesh
[2]Department of Arts and Sciences, Faculty of Engineering, Ahsanullah University of Science and Technology, Dhaka-1208, Bangladesh
[3]X-Ray Imaging and Computed Tomography, German Cancer Research Center, Im Neuenheimer Feld 280, 69120 Heidelberg, Germany
[4]Fluid Dynamics & Turbo-machinery Laboratory, Department of Mechanical Engineering, University of the Peloponnese, Patras, Greece
[5]Department of Mathematics, Section of Applied Mathematics and Engineering Research, University of Ioannina, Ioannina 45110, Greece

[a)]**Author to whom correspondence should be addressed:** ferdows@du.ac.bd

ABSTRACT

A conventional invasive catheterization procedure is currently used to detect atherosclerotic severity in coronary arteries. However, it is still challenging to measure multiple consecutive stenoses (MCS) in coronary main arteries, a severe condition, by using the invasive method. In this paper, we report important hemodynamic properties such as wall shear stress (WSS) and velocity magnitude (VM) across different luminal areas of coronary stenosis in patient-based right coronary artery models of MCS using pulsatile heart flow simulations. The hemodynamic factors in coronary blood flow simulations of different degrees of stenosis indicated a relationship between the proximal moderate stenosis and distal severe stenosis models. The results show the physical effects of different hemodynamic factors including VM, mean arterial pressure difference, WSS, and virtual fractional flow reserve (vFFR), which allow for predicting the physiological computation in the MCS artery severity conditions. This study identifies the fundamental physics of coronary plaque with MCS and indicates the impact of these factors on vFFR measurements. These findings provide insights into and improvement of the pathophysiological assessment of MCS. The results reveal hemodynamic properties, which can be used to diagnose coronary irregularities using a visualization method.

NOMENCLATURE

C_T	Capacitor
I	Identity vector
P_{dis}	Distal stenotic pressure
P_{pro}	Proximal stenotic pressure
P_{ven}	Venous pressure
$P(t)$	Blood pressure
$P(\omega)$	Fourier mode of the heart pressure
$Q(t)$	Heartbeat rate
R_1	Proximal resistance
R_2	Distal resistance
R_1+R_2	Total resistance
Re	Reynolds number
T	Periodic time of the heart flow rate
$\mathbf{u}$	Blood velocity
$z(t)$	Kernel function
$Z(\omega)$	Impedance of coronary artery
κ	Dilation viscosity
μ	Dynamic viscosity

ν	Kinematic viscosity
ρ	Blood density
τ	Wall shear stress
$\nabla \mathbf{u}$	Gradient velocity vector

I. INTRODUCTION

Performing coronary revascularization of multiple consecutive stenoses (MCS) in a single main branch of the coronary artery depends on several factors: narrowness of the lumen, type of stenosis (concentric or eccentric), and locations of stenosis. Serial stenoses in the major branch of the coronary artery are affected by the hemodynamic factors of other proximal or distal stenoses.[1,2] The presence of proximal moderate to distal severe stenosis or distal moderate to proximal severe stenosis significantly influences the downstream hemodynamic forces such as the heart flow pattern, wall shear stress (WSS), velocity magnitude (VM), time-average pressure difference, and virtual fractional flow reserve (vFFR). It is challenging to functionally assess MCS in the main coronary artery branch using the prevalent catheterization method.[3] The anatomical severity of coronary disease has been shown to be related not only to the area of coronary stenosis (ACS) but also to the location, type (eccentric, symmetric, or concentric), and length of the stenosis, which can affect the hemodynamic properties.[4,5] A series of right coronary artery (RCA) models have been created by adding single or one stenosis and MCS from 60% to 90% ACS on the baseline patient's data. In this study, we investigated the effect of the size of ACS, stenosis length, locations, types, and hemodynamic parameters. We also demonstrated that VM and WSS values provide an alternative approach to determining the FFRct and invasive FFR in this work. These findings can support physicians in deciding whether to perform a coronary revascularization procedure.

The coronary main branches supply oxygenated blood to myocardial muscles. Myocardial infarction is a significant risk in coronary revascularization of ischemia-related coronary lesions.[6,7] Coronary revascularization can restore patients' heart flow physiological conditions following the noninvasive treatment.[8] The obstruction of proximal (moderate) stenosis to distal (severe) stenosis can lead to interrupted blood flow in regions downstream of the stenosis.[9] A previous study demonstrated that a distal stenosis has a trivial effect on the disturbed flow pattern in the region upstream from the proximal stenosis in the main artery with 75% ACS. Li *et al.*[10] investigated the impact of a distal stenosis compared to a proximal stenosis in MCS RCA models within a coronary idealized model and in an experimental (*in vitro*) approach. In this study, we developed a computational relationship between the hemodynamic properties of distal and proximal stenoses in patient-based RCA hyperemia blood flow conditions. We considered four different categories of ACS models: moderate for 60% ACS, severe for 80% ACS, critical for 90% ACS, and in between moderate and severe for 70% ACS in patient-based RCA models.

Atherosclerosis plaques generally occur near bifurcations and bending regions of coronary vessels, which results in obstruction of blood flow in myocardial muscles.[11–13] Factors contributing to the development of atherosclerosis are quite complex in arteries affected by MCS; therefore, hemodynamic properties can be used to predict the flow conditions in individual patients.[14] The blood flow in coronary main arteries with MCS is complex and cannot adequately be assessed by visual interpretation of the conventional coronary angiogram.[15] Computational hemodynamic (CH) parameters were shown in one research study to have an imperative role in assessing the formation and development of the physiological blood flow conditions in cardiovascular irregularities.[16] The authors of this study demonstrated that RCA with or without branches does not affect the simulation results in the simulation of blood flow in coronary main arteries. The hemodynamic factors of each stenosis are influenced by others, indicating the significance of MHD, estimating the CH constraints of each coronary lesion.[17–19] CH parameters such as VM with streamlines, WSS, and vFFR offer the possibility of analyzing the local atherosclerotic plaque conditions in the main branch of the coronary arteries, which is difficult to access experimentally.[20,21] Previous research has produced numerical heart flow computational results in a single stenosis of a coronary artery by using different computer-aided design (CAD) and computational fluid dynamics (CFD) commercial tools. Additionally, many researchers have worked on different approaches (FSI) for heart flow simulation.[22–24]

Currently, FFR is a measure that is assessed during a wire-based catheterization procedure, which is the gold standard for estimating the hemodynamic features of coronary lesions; as a result, this procedure is recommended for making clinical decisions before coronary revascularization.[25] However, the high cost of guiding management and the risk of an invasive medical operation may impede the use of FFR measurements in the clinic.[26] It is also worth mentioning that two-thirds of the patients who underwent percutaneous coronary intervention (PCI) did not need coronary revascularization procedures in one study.[27] The clinical FFR is a complex measure, and the test outcome is not satisfactory in main coronary arteries with MCS. The numerical blood simulation in the MCS coronary heart flow varies in the downstream flow due to the spacing between the two consecutive stenoses and influences hemodynamical magnetic parameters.[28,29] A coronary computed tomography angiogram (CTA) along with advanced machine learning tools is presently used to produce CH results that enrich diagnostic assessments by illustrating the functional response of the hemodynamic properties.[10] CH parameters such as VM with streamlines, time-average pressure difference, WSS, and vFFR allow for predicting the physiological heart flow assessment that can be applied to measure the severity of the coronary lesions.

The boundary condition (BC) is a crucial parameter for assessing the physiological heart flow physics in patient-based coronary artery models.[30,31] The inflow and outflow boundaries critically impact the results of numerical simulations. Recently, a significant area of focus has been identifying appropriate BC specifications necessary to capture unique characteristics of coronary physiology. The lumped parameter models appropriately mimic diastolic governing flow, in which flow and pressure waveforms are out of phase due to cardiac contraction.[32] In this study, we have introduced explicit periodic BCs along with lumped features in the patient-based models. The heart pressure and flow rates are periodic in time, $T = 0.8$ s. The periodic cardiac cycle reflects a patient heart rate of 75 bpm. The explicit lumped parameter BCs are useful for pulsatile flow computations. The MCS flow pattern in a single main coronary is more complex than a single stenosis artery. WSS has a major impact on the endothelial vessel function, which plays a key role in both atherosclerotic disease progression and healing of vessels treated by intravascular mechanisms of coronary arteries.[33–35] The WSS gradient measures the spatial differences in hemodynamic forces on the vessel walls.[18,19]

The purpose of this study is to explore the hemodynamic properties of different degrees of ACS with MCS in pulsatile flow conditions. We set up an open-source technique that provides the CH parameters. The parameters indicate that each stenosis is affected by others in the main branch of the artery with MCS. We also explored the relationship between the flow rate and WSS distribution in 3D patient-based models with MCS. The hemodynamic property relationship in the MCS models produces the proximal severe (80% ACS) stenosis to distal moderate (60% ACS) stenosis and the distal severe stenosis to proximal moderate stenosis. In practice, it is signified by the pressure ratio between the coronary artery region distal to the plaque and the ostium pressure drop across a stenosis during hyperemia, when the coronary arteries are extensively dilated using adenosine. We observed that the MCS model produced results for the moderate to severe stenosis models, which is discussed in detail in Sec. IV.

Scheme 1 presents the outline of this study.

In the present work, we implemented several methods for patient-specific heart flow simulations, including medical image (CTA) acquisition, appropriate segmentation, suitable surface generation on 3D and model reconstruction, consistent mesh generation, computational simulation, and result analyses. The study is ordered as follows: in Sec. II, the detailed methodologies are discussed, and physiological BCs and numerical approaches are illustrated in Sec. III. In Sec. IV, the detailed CH results, for instance, the flow pattern, WSS, pressure distribution, flow rate, and vFFR, are presented on a series of patient-based RCA models. Finally, conclusions were drawn in Sec. V.

II. METHODOLOGY

A. CTA medical image acquisition

According to 2019 heart disease and stroke statistics provided by the American Heart Association, cardiovascular disease is the number one killer in the world. Furthermore, coronary artery disease is an increasingly important cause of morbidity and mortality in Bangladesh.[36] The medical image data acquisition was performed in a home hospital (SQUARE Hospital, Dhaka, Bangladesh) by following some of the parameters described in the study by Hoque *et al.*[1] The volume of the dataset used for this study had a voxel size of 512 × 214 × 512.

Target patient characteristics:

Patient: sex—male, BMI—25.5, and age—67 years	Hypertension: yes
Shortness of breath: yes	Previous myocardial infarction: no
Diabetes: yes	Percutaneous coronary intervention: no

We employed open-source tools[37] for the medical image segmentation, model surface creation, construction of patient models, and heart flow simulations. The hemodynamic heart flow results were

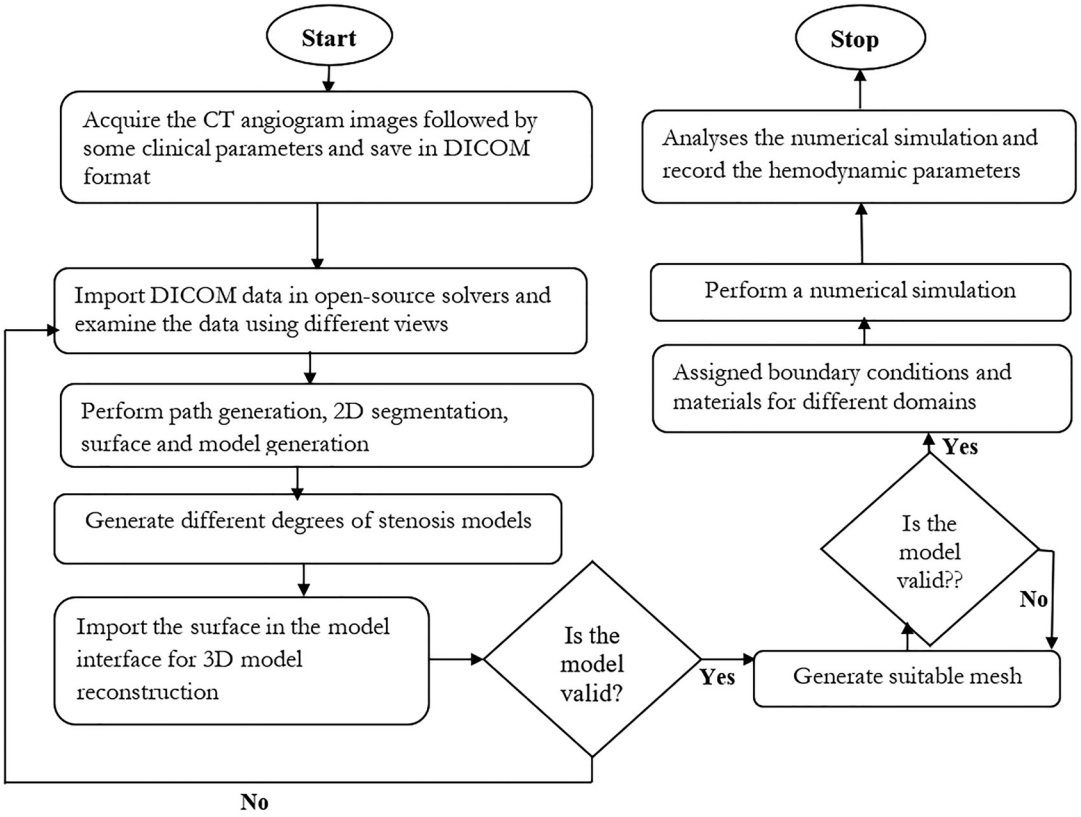

SCHEME 1. The outline of the study.

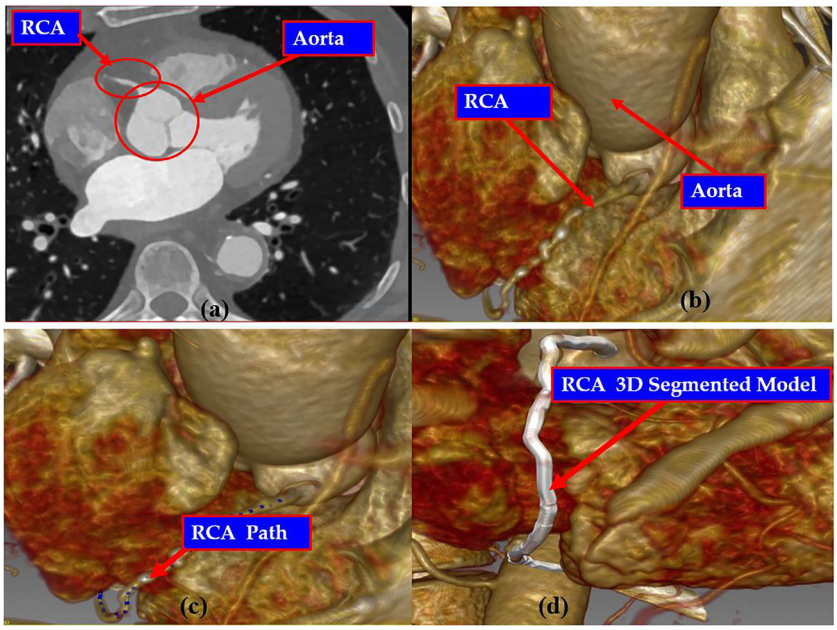

FIG. 1. (a) A slice with the aorta and RCA, (b) rendered volume of the anatomical view of RCA and aorta, (c) RCA model path generation, and (d) geometry of surface generation from the routine CTA data, which is based on the previous literature.[1]

investigated by utilizing Paraview.[38] First, the CTA data in the DICOM setup were imported into the main workbench; see Fig. 1(a). We adopted the methods described in the previous literature[1] for RCA path generation and model segmentation.

B. 3D geometry reconstructions

Generating the appropriate patient-specific geometry is a challenging task for simulating the pathophysiological heart flow. Morphological changes in the vascular anatomy are commonly associated with the clinical diagnosis and calculation of blood flow in major coronary arteries.[39] RCA models with various volumes of plaque are produced by using a semiautomatic subdivision procedure. In this work, a patient dataset with eleven different cases (healthy, single stenosis with different degrees of stenosis, and multiple stenoses with moderate to critical cases) was studied. It is largely acknowledged that the coronary artery bifurcation and curving areas are susceptible to the development of atherosclerotic stenoses. Single and multiple stenoses were generated with different arbitrary ACS sizes from moderate to severe stenosis in different locations, particularly in the bending regions [Figs. 2(b)–2(k)] in the patient RCA models. The ACS is calculated using the following equation:[40]

$$\text{Percentage of ACS} = \left[1 - \left(\frac{R_{\text{stenosis}}}{R_{\text{normal}}}\right)^2\right] \times 100\%. \quad (1)$$

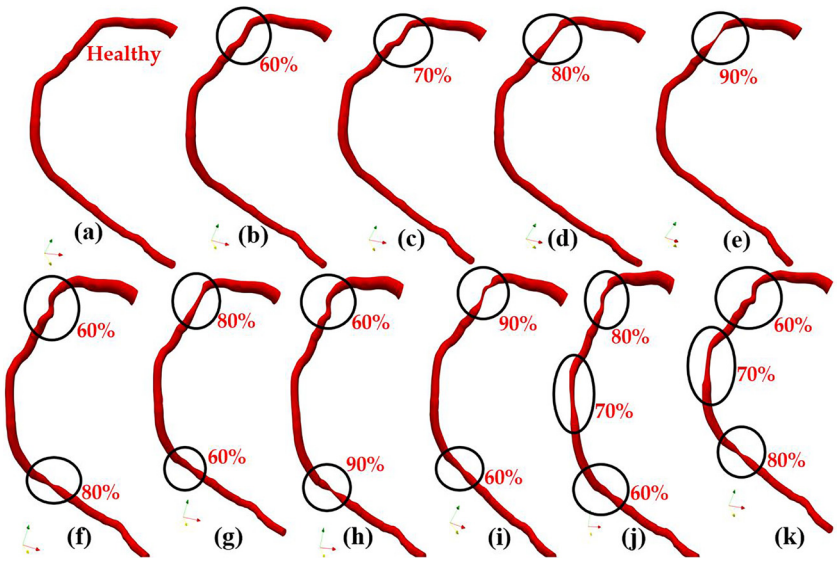

FIG. 2. (a) The healthy patient RCA model, (b)–(e) a single stenosis with different ACS models, and (f)–(k) various sizes of MCS models.

Here, $R_{stenosis}$ and R_{normal} indicate the radii of disease and normal (nondisease) areas, respectively, in the patient model. The RCA contains one inlet, one outlet, and a wall with different sizes of stenosis areas, as shown in Fig. 2. The surfaces of the RCA models are smoothed by applying local and global constraint parameters. The radii of the inlet and outlet of the RCA models are 1.75 mm and 0.87 mm, respectively. The total area of the coronary artery wall is $1000 \pm 200\ mm^2$, and the length of the model is ≈12 cm.

It has been clinically recognized that eccentric, long symmetric, asymmetric, and concentric stenoses are often built in the coronary artery main branches. Waller[41] demonstrated that 73% of the atherosclerotic plaques in the coronary lumen were eccentric and 27% were concentric. Figures 2(b)–2(e) show the single stenosis models with 60%–90% ACS, respectively, of the RCA main twig. 60% and 70% ACS models are eccentric, and 80% and 90% ACS models are long symmetric and concentric patient-based RCA models. Figures 2(f)–2(k) show the MCS models with the proximal moderate 60% ACS to the distal severe 80% ACS and critical 90% ACS and the distal moderate 60% ACS to the proximal severe 80% ACS in the RCA models. The second stenosis [Figs. 2(f)–2(k)] is built from the ostium of the RCAs, which is also concentric, and the third stenosis [Figs. 2(j)–2(k)] is considered to nearly be an eccentric stenosis. The outputs are presenting a proportional relation with a noninvasive calculation of vFFR values and patients' model ACS severity. Computational simulations were carried out in these eleven models to mimic the hemodynamic conditions in both the diseased and healthy patient RCA models.

C. Competitive grid generation

Grid generation is important to facilitate the physical solution of partial differential equations (PDEs) in the patient models. Finite element grid generation provides a concise and comprehensive technique over bending surfaces and volumes.[42,43] The grid of the geometries was produced by using a nonstructural mesh with tetrahedral elements. The isotropic mesh was specified in the 3D computational domains with specific parameters, such as global maximum edge size (0.3 cm, for fine mesh), followed by advanced options for all RCA models. In the advanced options, we added four boundary layers in the computational domain wall, an edge element sized 0.35 cm, and a layer decreasing ratio of 0.8. The total number of meshes in the original patient RCA model was approximately $6 \pm 2 \times 10^4$. Figure 3(a) shows the magnified views of the important mesh parts of the RCA model, and Fig. 3(b) represents the mesh convergence test results of the RCA model.

A mesh independence test for VM was performed for various mesh densities. The mesh sizes ranged from very coarse (number of elements: 13 320) to fine (148 732 elements). The grid of the geometries was produced by the finite element method. The grid test produced a 0.85% difference in the coarse grid compared to the smaller size grid (fine grid).

III. FUNCTIONAL BOUNDARY CONDITIONS AND NUMERICAL SIMULATIONS

Accurate boundary conditions (BCs) are crucial for obtaining high-quality physiological heart flow simulation in patient-specific coronary models. Several researchers have used different types of BCs including analytic BCs, implicit and explicit BCs, lumped parameter models, Windkessel (WK) models, or low-dimensional models, leading to multiscale approaches.[44–46] Du *et al.*[47] showed that explicit BCs produced an appropriate simulation of patient functional blood flow. Here, we have utilized explicit BCs along with lumped constraints in the RCA models. Since the human heart rate is almost periodic, we adopt that the heart pressure and flow are periodic in time, with period T,

$$\text{i.e.,}\ P(x,0) = P(x,T) \quad \text{and}\ Q(x,0) = Q(x,T), \tag{2}$$

where we set up the duration of a single heart rate, T = 0.8 s.

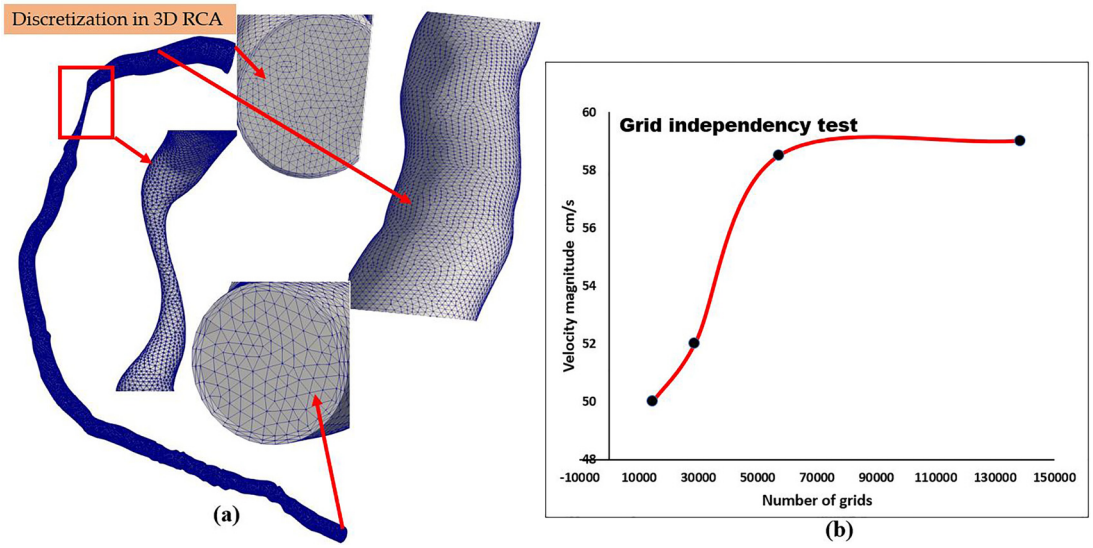

FIG. 3. The tetrahedral grid, inlet, stenosis regions, bending, and outlet are shown above. The grid convergence test resulted in several grids (fine, coarse, coarser, and very coarse) for the RCA models.

Du *et al.* illustrated that there is a linear connection between heart pressure and flow at the outlet of the coronary main arteries during the periodic cardiac output. In the Fourier space, the outlet boundary condition satisfies

$$P(\omega) = Q(\omega)Z(\omega), \tag{3}$$

where $P(\omega)$ is the Fourier mode of the heart pressure of P(t) and $Z(\omega)$ is the impedance of the truncated coronary artery. The above equation can be written as

$$P(t) = \frac{1}{T}\int_{t-T}^{t} z(t-\zeta)Q(\zeta)d\zeta, \tag{4}$$

where $z(t)$ is the kernel function, which is the inverse Fourier transform of $Z(\omega)$. We apply the three-element Windkessel (WK) model for the outflow boundary in the outlet section.

A comprehensive hemodynamic assessment of the interrupted, the spatial, and the temporal flow patterns may provide more insight into understanding the development of atherosclerosis and have an imperative clinical value. However, it is hard to assess local flow patterns and mechanical forces *in vivo* with adequate accuracy. Computational models provide a useful tool in that regard.[47]

A. Inlet boundary conditions

It is crucial that accurate BCs capture the physical blood flow conditions in the vascular 3D models. In this study, we have employed the inflow velocity profile, shown in Fig. 4(a), for pulsatile flow conditions. The flow going into the 3D patient coronary models is negative because the normal vector at the inlet points outwards. The explicit inlet velocity waveform produces a pulsatile behavior in the arterial domain.

B. Outlet boundary conditions

We have prescribed an outlet pressure waveform, shown in Fig. 4(b), which is continuous over the outlet face in a weak manner. By enforcing the integral of the pressure field on that surface, the pressure waveform must be of a positive value. There are three elements that WK coronary BCs introduce at the RCA outlet. The WK model describes the relationship between the heart flow and the pressure at the outlet of the RCA models. The WK three-element model produces a similar analogy to an electric circuit in Fig. 4(c). In the WK model, the blood pressure, P(t), agrees with the voltage of the electric circuit, and the heartbeat rate, Q(t), corresponds to the electric current and a proximal resistance (R_1) model. The capacitor (C_T) utilizes the viscous resistance and vessel compliance of all the arterial downstream of the vascular models and the distal resistance (R_2) is the resistance of the capillaries and venous circulation. Du *et al.* stated that the heart pressure and flow proportion in the three-element WK model clearly satisfy Kirchhoff's law

$$\frac{dP(t)}{dt} + \frac{P}{R_2C_T} = R_1\frac{dQ(t)}{dt} + \frac{Q(R_1+R_2)}{R_2C_T}, \tag{5}$$

where R_1+R_2 and R_1 are the total resistance and the characteristic resistance, respectively.

A modified and explicit lump parameter model, shown in Fig. 4(c), has been used in patient-based models to control the out of phase nature of coronary flow and pressure conditions. The WK model and outlet waveform include the intramyocardial pressure, which maintain the coronary circulation to be out of phase in the systemic circulation. The resulting models effectively captured typical physiological flow characteristics of the coronary circulation.

C. Numerical methods

The blood flow in coronary main arteries with MCS is quite complex and cannot be easily assessed by visual interpretation of the invasive coronary angiogram. The blood flow simulations are directed by a set of pathophysiological BCs and parameters in the RCA models.

Blood flow is considered to be laminar and pulsatile, and the blood is an incompressible and Newtonian fluid, as generally recognized in large vessels.[48] The following appropriate rheological constraints were applied with density, $\rho = 1060\,kg/m^3$, and kinematic

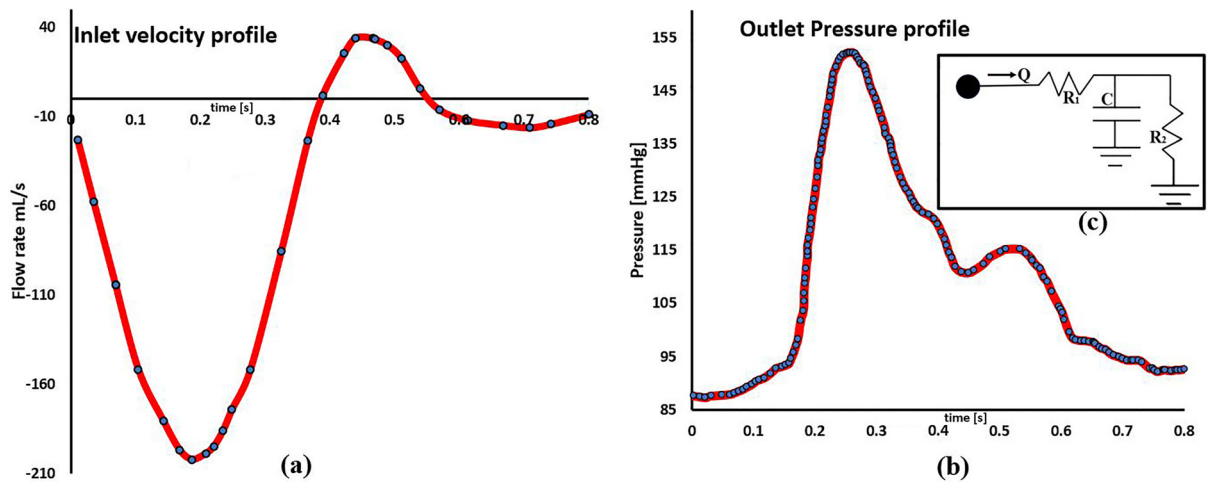

FIG. 4. (a) Inlet velocity, (b) outlet pressure profiles, and (c) three-element Windkessel models are introduced in patient models for CH simulations. The waveforms imitate the transient performance of the inlet and outlet pathophysiological states. The images (a) and (b) have been described in the literature.[1]

viscosity, $\nu = 3.7736 \times 10^{-6}$ m^2/s.[49,50] We also assume that the heart flow is periodic where the cardiac cycle period is T = 0.8 s in the models.

We know that blood exhibits non-Newtonian behavior in capillaries or small radius coronary arteries.[51] Several studies have demonstrated that non-Newtonian and Newtonian blood flow simulation results are similar in the main branches of the coronary arteries.[48]

The computational results obtained by solving the momentum and conservation of mass equations, i.e., the three-dimensional Navier–Stokes equations with the continuity for incompressible fluid, are

$$\frac{\partial \mathbf{u}}{\partial t} + (\mathbf{u}.\nabla)\mathbf{u} + \frac{\nabla P}{\rho} - \nu \Delta \mathbf{u} = 0, \quad \text{div}\,\mathbf{u} = 0, \tag{6}$$

where P, $\mathbf{u}$, ν, and ρ are the pressure, velocity vector, kinematic viscosity, and density of the patient's blood, respectively. For solving the nonlinear system of PDEs, we impose a set of BCs like no-slip for the coronary artery wall, outlet pressure, and inlet fluid flow waveforms (Fig. 4) along with the three-element WK model at the outlet in the RCA models for CH simulations.

$$\text{The Stokes relation } \tau = \mu\left[\nabla \mathbf{u} + (\nabla \mathbf{u})^T\right] + \left(\frac{2}{3}\mu - \kappa\right)(\nabla.\mathbf{u})I \tag{7}$$

applies to the WSS measure, where $\nabla \mathbf{u}$, κ, and I are the gradient of the velocity vector, dilatational viscosity, and identity vector, respectively. Lumped constraints are applied for directing the overall outflow of distal microvascular resistance.

Finally, the vFFR is formulated by the following equation:

$$\text{vFFR} = \frac{P_{dis} - P_{ven}}{P_{pro} - P_{ven}}, \tag{8}$$

where P_{dis} and P_{pro} are time-averaged distal and proximal stenotic pressures and P_{ven} is the venous pressure at zero in Pa.[2,52]

IV. RESULTS AND DISCUSSION

The heart flow of the VM and WSS values was estimated for various degrees of ACS models at definite times and positions of the RCA domains. The pulsatile waveforms (Fig. 4) introduced hemodynamic properties in the numerical simulation.

A. Wall shear stress (WSS)

Low and high WSS magnitude values play a driving role in the formation and development of atherosclerotic plaques in patient coronary arteries.[53] The tangential stress gradients compute the spatial variations in hemodynamic intensities of the vascular wall.

Figure 5 shows the differences in WSS magnitude values in the various models. We observed that the WSS values in the stenosis regions are relatively higher than those in the unstenosed areas. Figure 5(a) shows the WSS values in the healthy model. It is quite clear that the WSS magnitudes are very consistent over the vessel wall, and the values vary from 18 to 25 Pa. Figures 5(b)–5(e) show the WSS results in the single stenosis models across various sizes and locations of the RCA domains. In contrast, Figs. 5(f)–5(k) illustrate the WSS values in

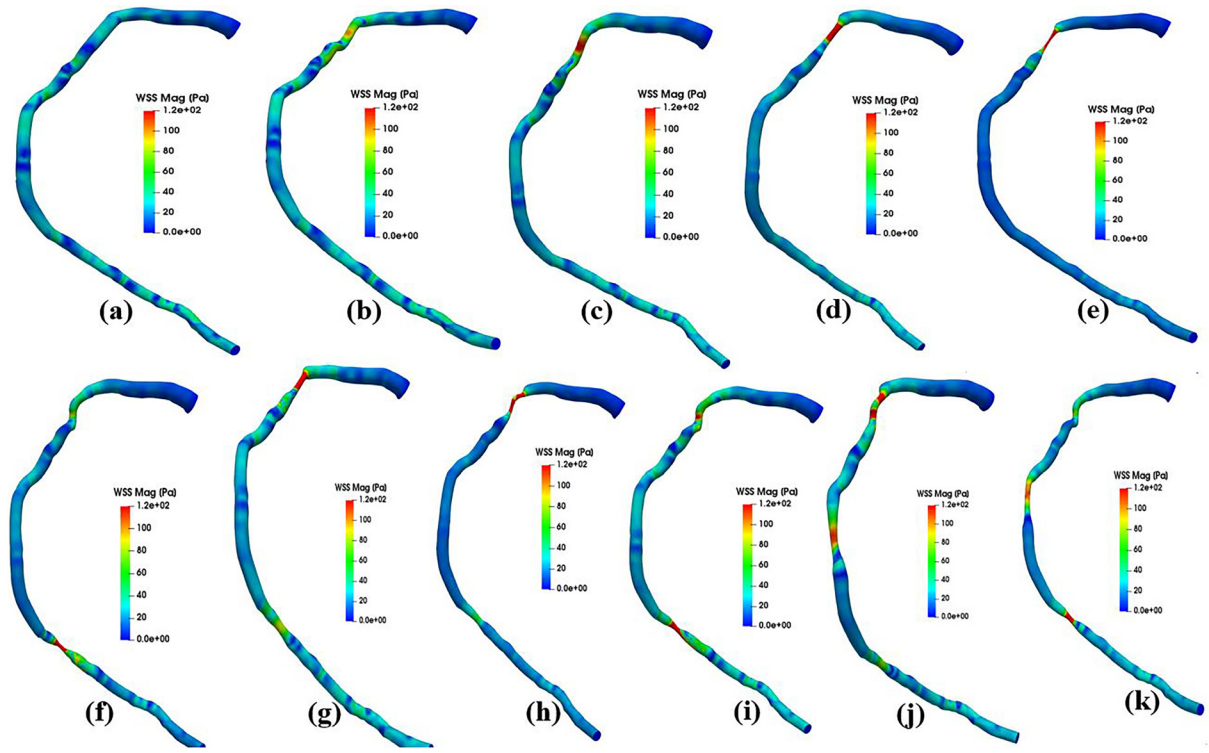

FIG. 5. (a)–(e) The WSS results in the (a) healthy and single stenosis models with (b) 60% ACS, (c) 70% ACS, (d) 80% ACS, and (e) 90% ACS (upper row), respectively. (f)–(k) The MCS models with moderate 60% ACS to severe 80% ACS in the bottom row.

the MCS models across diverse sizes and positions of the RCA computational models. In Figs. 5(b)–5(e), the diseased region exhibits high WSS magnitudes such that 60% stenosis corresponds to a WSS magnitude of 80–90 Pa, 70% to 90–100 Pa, 80% to 100–120 Pa, and 90% to over 120 Pa in single stenosis domains where the upper or lower regions of the stenosis show very low WSS values [less than 30 Pa]. Moreover, in the MCS domains [Figs. 5(f)–5(k)], the WSS magnitudes are more visible in the diseased areas. Hence, the WSS differs considerably in the disease areas compared to the unstenosed areas.

B. Velocity magnitude with streamlines

At the inlet, blood flow is laminar with Reynolds number Re = 387.45, but in different ACS regions, the Reynolds number increases in the diseased areas. In the 60%–90% ACS models, the Reynolds numbers are Re = 482.3, 675.75, 954, and 1017.6, respectively. Some researchers[54] have indicated that the critical Reynolds number in the coronary artery is 500. Above the critical number, the blood flow exhibits turbulent nature.[55] In this study, it is obvious that in stenosis areas greater than 60% ACS, the flow could be considered to be turbulent; however, an additional study is required in these regions.

Figure 6 represents the VM with streamlines in the RCA models with various sizes of stenosis. Figure 6 depicts the relative mean flow difference in pulsatile heart flow simulations. The VMs are relatively higher in the stenosis areas than in the unstenosed ones. Figure 6(a) presents the VM result in the patient model. It is quite clear that the VM values are the same over the coronary vessel wall, and the values range from 40 to 45 cm/s. Figures 6(b)–6(e) show the VM outcomes in the single diseased domains across a variety of sizes of stenoses and in different positions of the RCA models. Figures 6(f)–6(k) show the VM with streamline results in the MCS diseased models with different magnitudes of stenoses and in different positions in the patient models. In Figs. 6(b)–6(e), the throat (stenosis) region displays a high relative VM (greater than 300–900 cm/s) in one stenosis model where the upper or lower stream areas show very low magnitude values (less than 40–60 cm/s). In the multiple stenosis models [Figs. 6(f)–6(k)], it is more noticeable that the relative VM is too high in the stenosis areas. Consequently, the VM results vary distinctly in the diseased areas than in the unstenosed areas in the RCA domains.

C. Simulation result discussion

In this section, we discuss the numerical comparison results of the time-average WSS and VM values in the healthy, single stenosis and MCS models. Figures 7(a)–7(c) represent the WSS and VM values in the hyperemia flow pattern in the patient healthy model.

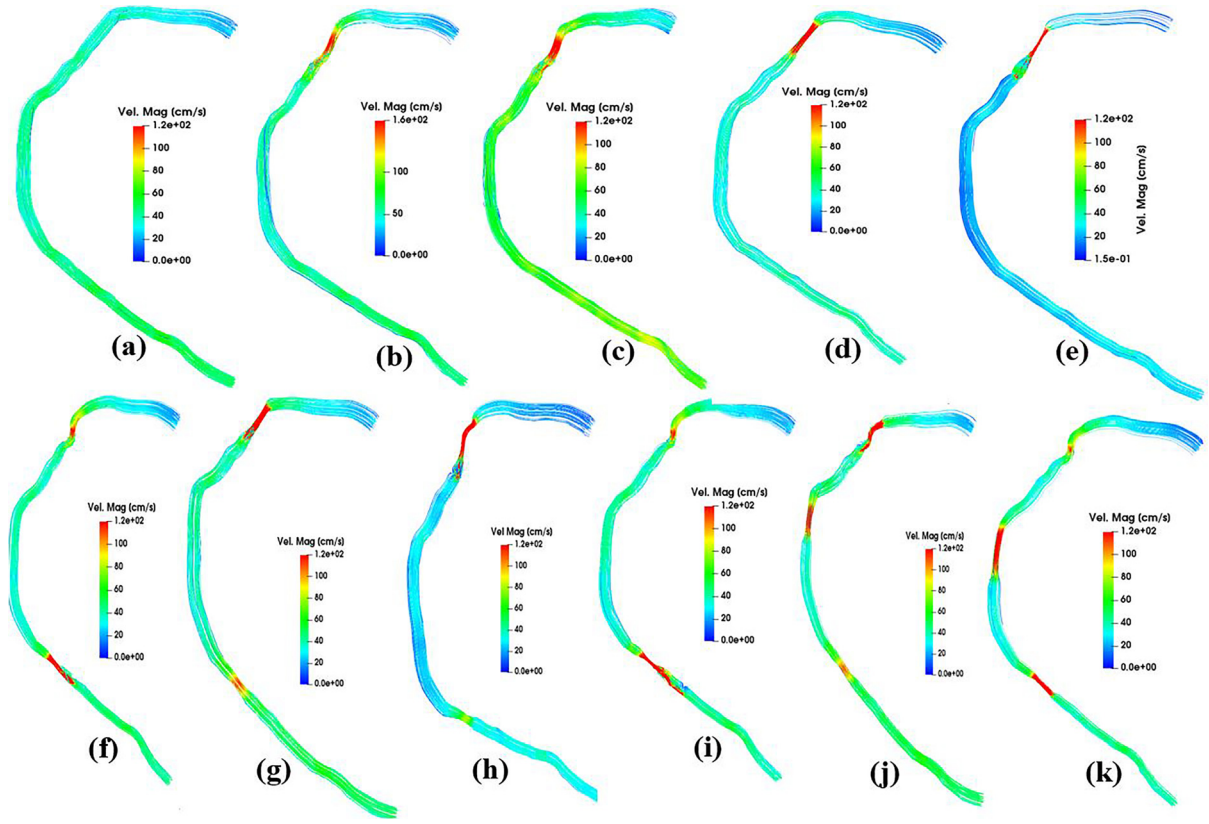

FIG. 6. Comparison of simulation results of the VM with streamlines in (a) the healthy, single stenosis model with (b) 60% ACS, (c) 70% ACS, (d) 80% ACS, and (e) 90% ACS and the MCS models with moderate to severe stenoses in the bottom row.

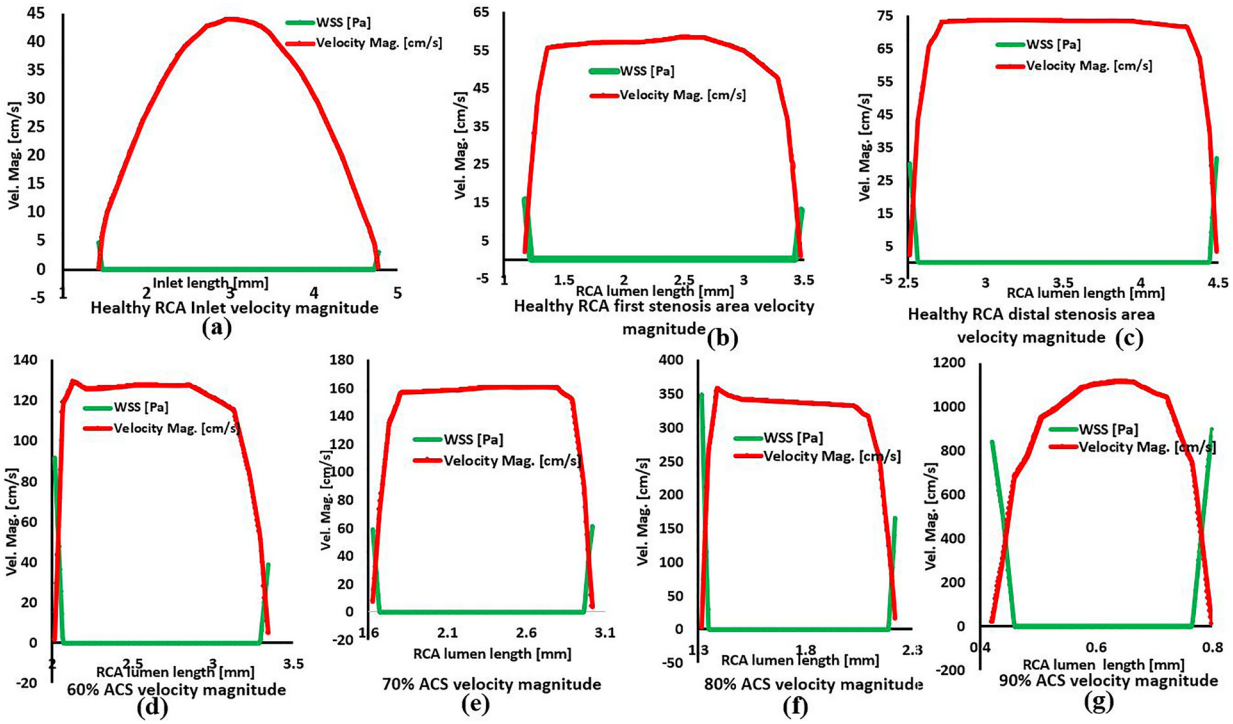

FIG. 7. (a)–(c) The velocity and WSS magnitude values in the healthy model. (d)–(g) The same parameters in proximal stenosis locations with 60%–90% ACS.

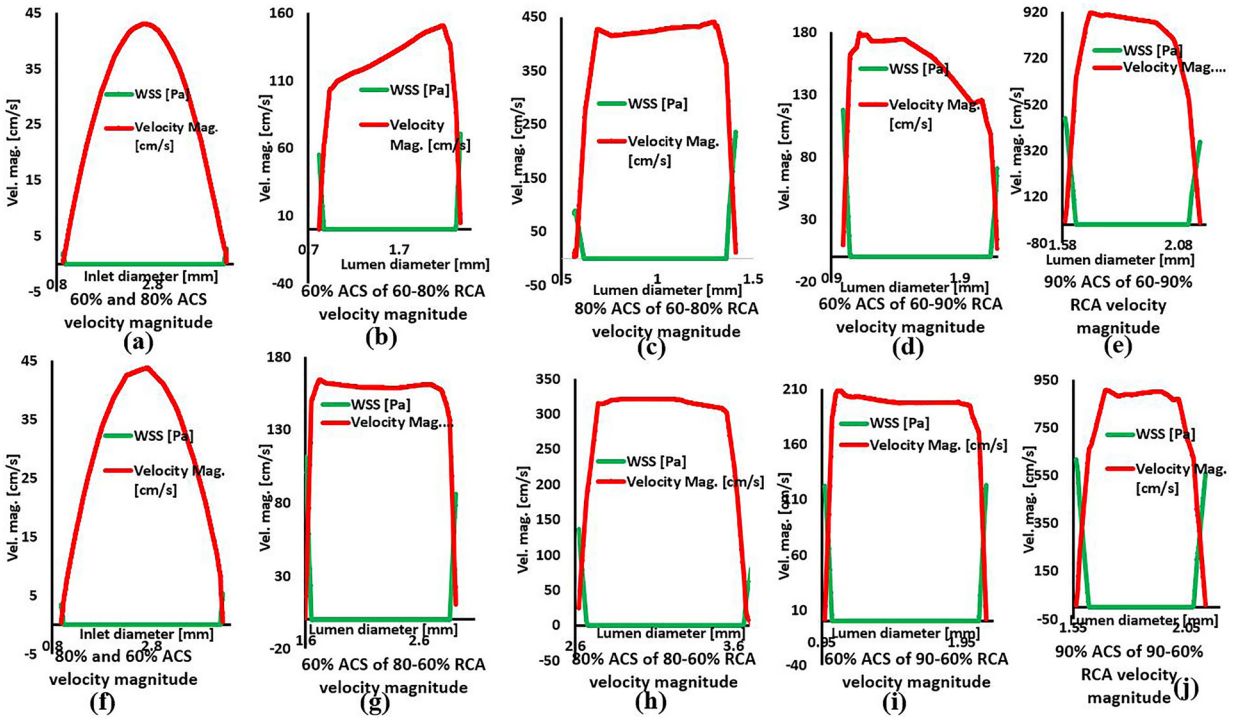

FIG. 8. (a)–(j) The velocity and WSS magnitude values in the MCS models in [(b) and (f)] the inlet and proximal and distal areas with moderate 60% ACS to severe 80% ACS and critical 90% ACS models.

Figure 7(a) shows that the inlet blood flow magnitude is ≈43 cm/s and WSS is ≈ 5 Pa.

Figures 7(b) and 7(c) show that the velocity and WSS magnitudes are 57 cm/s, 75 cm/s, and 15 Pa, 30 Pa in the proximal and distal stenosis locations, respectively, in the healthy model. The flow in the healthy model represents a laminar flow pattern in these positions.[54] Figures 7(d)–7(g) illustrate the WSS and VM values in the hyperemia flow pattern in 60%–90% ACS RCA models. We observed that the WSS and VM values were consistently increasing from the moderate (60%) to severe (70% and 80%) and to critical (90%) ACS conditions of the RCA models. More precisely, our simulation results showed that the wall tangential values (green color in the figures) obtained the highest values close to the wall as the percentage of stenosis increased. The highest WSS values were observed for 90% ACS in the single stenosis model.

Figure 8 shows the WSS and VM values of the hyperemia blood flow condition in the patient-based moderate (60%) to severe (80%) and to critical (90%) MCS models.

In the proximal 60% ACS and distal severe 80% ACS models [Figs. 8(b) and 8(c)], the results showed that the VM was 150 cm/s and 450 cm/s, whereas the mean WSS magnitude was 63 Pa and 140 Pa, respectively.

Figures 8(g) and 8(h) represent the average WSS and VM values of severe to moderate ACS; the values of velocity were 165 cm/s and 310 cm/s, and the WSS values were 40 Pa and 105 Pa, respectively. These results indicate that the proximal moderate (60%) stenosis and the distal severe (80%) stenosis in the MCS models are significant for atherosclerotic disease progression. In contrast, Figs. 8(d) and 8(e) show the proximal moderate (60%) and distal critical (90%) ACS model simulation results. In moderate to critical stenosis model simulations, these figures show that the mean WSS values were 95 Pa and 480 Pa, and the velocity magnitude values were 180 cm/s and 920 cm/s, respectively. Conversely, Figs. 8(i) and 8(j) demonstrate the critical to moderate ACS model simulation results, which display the mean WSS values of 120 Pa and 580 Pa and the VM values of 210 cm/s and 940 cm/s.

The WSS and VM values of the MCS along with three consecutive stenoses through proximal 60% ACS and 70% ACS and distal 80% ACS, distal 60% ACS and then 70% ACS, and proximal 80% ACS of RCA models are displayed in Fig. 9. Figure 9(a) depicts the inlet velocity and WSS magnitude values showing a laminar flow pattern. Figures 9(b)–9(d) illustrate the 60%–80% ACS WSS and velocity values in the moderate to severe stenoses model. Figures 9(b)–9(d) exhibit velocities that were 140 cm/s in 60% ACS, 270 cm/s in 70% ACS, and 450 cm/s in 80% ACS; the WSS values were 75 Pa, 145 Pa, and 210 Pa, respectively, in the MCS model.

Figures 9(e)–9(g) show that the velocities were 70 cm/s, 230 cm/s, and 340 cm/s, while the WSS values were 70 Pa, 85 Pa, and 150 Pa in 60%–80% ACS, respectively. Hence, it is apparent that the moderate to severe or severe to moderate ACS reveals similar outcomes for the two and three stenosis MCS models.

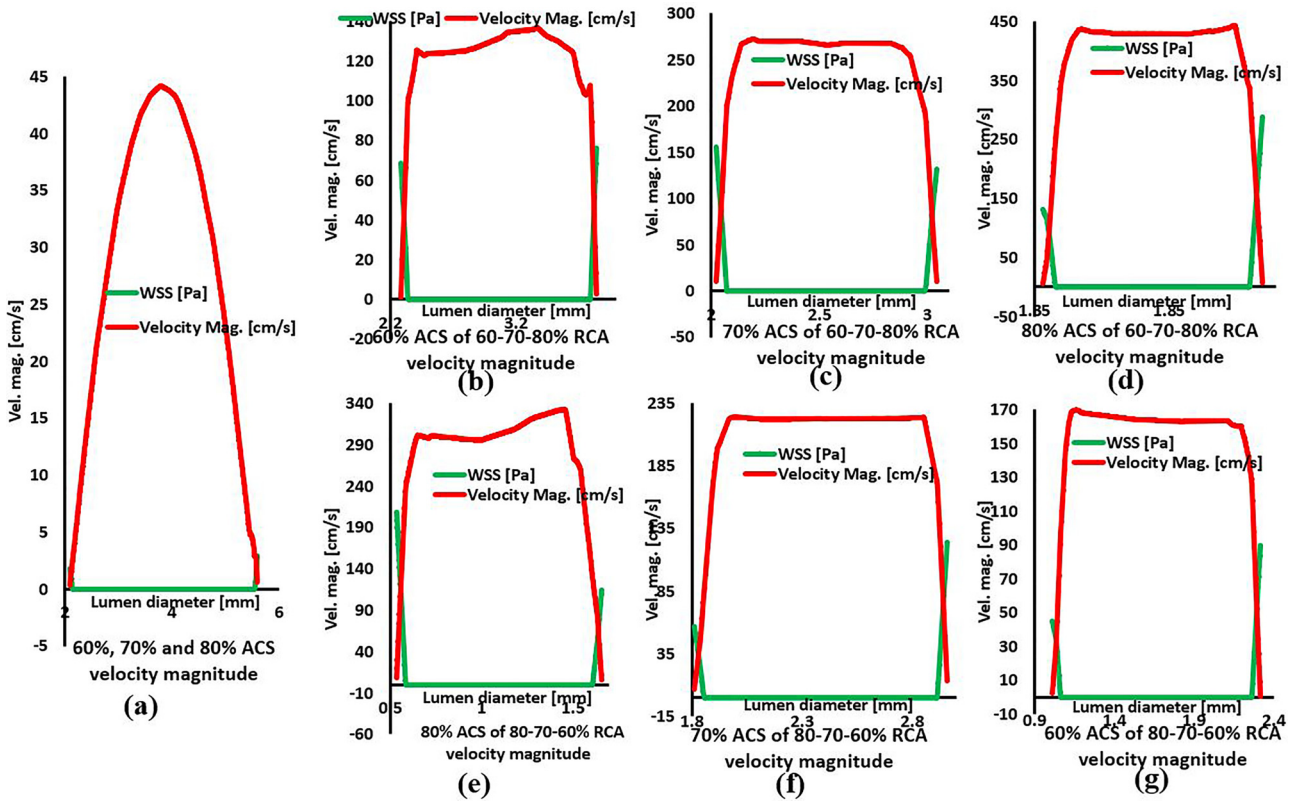

FIG. 9. (a)–(g) The velocity and WSS magnitude values in the MCS models in the (a) inlet and proximal and distal areas with moderate [(b) and (g)] 60% ACS to [(c) and (f)] 70% ACS to severe [(d) and (e)] 80% ACS.

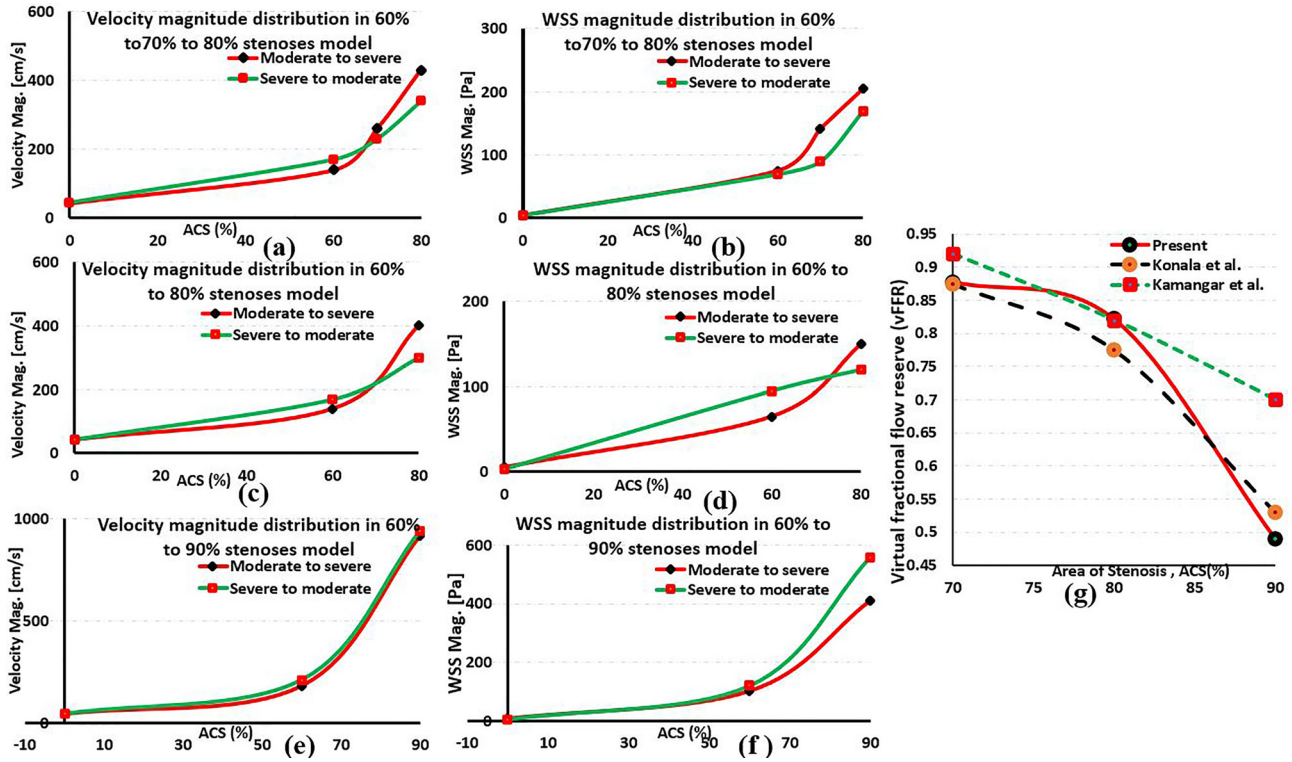

FIG. 10. (a)–(f) The numerical comparison results of average WSS and VM distributions between the severe and moderate MCS models and (g) the comparison results of vFFR.

Figures 10(a)–10(f) illustrate the graphical presentation of our simulation results. The MCS 60%–80% models show the WSS and VM values in Figs. 10(a) and 10(b). From this outcome, we could conclude that proximal moderate and distal severe (80%) stenosis cases reveal a higher flow rate and WSS magnitude. In the 60%–80% ACS stenosis case, we observed the same effect for moderate to severe and severe to moderate stenosis models. In contrast, Figs. 10(e) and 10(f) show that proximal critical (90%) stenosis and distal moderate stenosis are more significant for coronary revascularization. Therefore, the VM and WSS values introduce an alternative approach compared to the invasive procedure for coronary revascularization. Figure 10(g) shows a comparison of the computational results and published studies. In order to validate the numerical simulations, we compared the vFFR values of the 90%, 80%, and 70% ACS models with previously published research. The vFFR value of the single stenosis and MCS models is ≈0.871 and ≈0.783, respectively, which indicate that the MCS models are very substantial since the vFFR value is less than 0.8. Figure 10(g) shows that the outcomes of this study are similar to the findings of Konala *et al.*[56] and Kamangar *et al.*[57] The vFFR results produce clinically relevant information that is important for coronary revascularization.

V. CONCLUSION

This work provides a framework for predicting the physiological response of main coronary flow conditions of MCS by using a noninvasive method. We have employed appropriate BCs in the inlet and outlet with a three-element WK model. The pulsatile boundary profiles produced physiological behaviors in the healthy, single stenosis and MCS models. In the MCS coronary models, the proximal moderate and distal severe stenoses produced higher WSS and velocity values than the distal moderate and proximal severe stenoses. On the other hand, the proximal critical and distal moderate stenoses have shown higher WSS and VM than the distal critical and proximal moderate stenoses. These findings, proximal stenosis severity being more harmful than that of distal stenosis, may provide fundamental understanding of the impact of hemodynamic properties on coronary artery disease measurements. This understanding could provide insight into improving the pathophysiological assessments of MCS models. The results reveal CH factors that may be useful to physicians for diagnosing coronary abnormalities using a method of visualization. We hope that the results are feasible for clinical applications; however, there are some limitations to this procedure, which require additional studies. This noninvasive, low-risk, and less expensive technique could be utilized to predict the severity of coronary artery diseases.

ACKNOWLEDGMENTS

We are thankful to Dr. Mohammad Towhiduzzaman, Coordinator and Consultant, Department of Cardiology, Square Hospital Ltd., Dhaka, Bangladesh, for providing technical support for acquiring medical imaging data from the Dhaka local hospital.

DATA AVAILABILITY

The data that support the findings of this study are available from the corresponding author upon reasonable request.

REFERENCES

[1]K. E. Hoque, M. Ferdows, S. Sawall, and E. E. Tzirtzilakis, "The effect of hemodynamic parameters in patient-based coronary artery models with serial stenoses: Normal and hypertension cases," Comput. Methods Biomech. Biomed. Eng. **23**(9), 467–475 (2020).

[2]N. H. J. Pijls *et al.*, "Coronary pressure measurement to assess the hemodynamic significance of serial stenoses within one coronary artery: Validation in humans," Circulation **102**(19 SUPPL), 2371–2377 (2000).

[3]S. Ju and L. Gu, "Hemodynamic interference of serial stenoses and its impact on FFR and iFR measurements," Appl. Sci. **9**(2), 279 (2019).

[4]J. M. Zhang *et al.*, "Simplified models of non-invasive fractional flow reserve based on CT images," PLoS One **11**(5), e0153070 (2016).

[5]N. Freidoonimehr, R. Chin, A. Zander, and M. Arjomandi, "An experimental model for pressure drop evaluation in a stenosed coronary artery," Phys. Fluids **32**(2), 021901 (2020).

[6]L. Papamanolis *et al.*, "Myocardial perfusion simulation for coronary artery disease: A coupled patient-specific multiscale model," Ann. Biomed. Eng. (published online) (2020).

[7]P. D. Morris *et al.*, "Computational fluid dynamics modelling in cardiovascular medicine," Heart **102**(1), 18–28 (2016).

[8]B. L. Nørgaard *et al.*, "Diagnostic performance of noninvasive fractional flow reserve derived from coronary computed tomography angiography in suspected coronary artery disease: The NXT trial (Analysis of coronary blood flow using CT angiography: Next steps)," J. Am. Coll. Cardiol. **63**(12), 1145–1155 (2014).

[9]B. Liu and D. Tang, "Influence of distal stenosis on blood flow through coronary serial stenoses: A numerical study," Int. J. Comput. Methods **16**(3), 1842003–1842011 (2019).

[10]S. Li *et al.*, "Numerical and experimental investigations of the flow–pressure relation in multiple sequential stenoses coronary artery," Int. J. Cardiovasc. Imaging **33**(7), 1083–1088 (2017).

[11]S. Beier *et al.*, "Impact of bifurcation angle and other anatomical characteristics on blood flow—A computational study of non-stented and stented coronary arteries," J. Biomech. **49**(9), 1570 (2016).

[12]N. Zaman, M. Ferdows, M. A. Xenos, K. E. Hoque, and E. E. Tzirtzilakis, "Effect of angle bifurcation and stenosis in coronary arteries: An idealized model study," BioMed Res. J. **4**(3), 214–228 (2020).

[13]A. Passos, J. M. Sherwood, E. Kaliviotis, R. Agrawal, C. Pavesio, and S. Balabani, "The effect of deformability on the microscale flow behavior of red blood cell suspensions," Phys. Fluids **31**(9), 091903 (2019).

[14]R. Mittal *et al.*, "Computational modeling of cardiac hemodynamics: Current status and future outlook," J. Comput. Phys. **305**, 1065–1082 (2016).

[15]U. Siebert *et al.*, "Improving the quality of percutaneous revascularisation in patients with multivessel disease in Australia: Cost-effectiveness, public health implications, and budget impact of FFR-guided PCI," Heart, Lung Circ. **23**(6), 527–533 (2014).

[16]J. G. Myers, J. A. Moore, M. Ojha, K. W. Johnston, and C. R. Ethier, "Factors influencing blood flow patterns in the human right coronary artery," Ann. Biomed. Eng. **29**(2), 109–120 (2001).

[17]F. A. Alwawi, H. T. Alkasasbeh, A. M. Rashad, and R. Idris, "MHD natural convection of sodium alginate Casson nanofluid over a solid sphere," Results Phys. **16**, 102818 (2020).

[18]F. A. Alwawi, H. T. Alkasasbeh, A. M. Rashad, and R. Idris, "Heat transfer analysis of ethylene glycol-based Casson nanofluid around a horizontal circular cylinder with MHD effect," Proc. Inst. Mech. Eng., Part C **234**(13), 2569–2580 (2020).

[19]G. Palani and I. A. Abbas, "Free convection MHD flow with thermal radiation from an impulsively-started vertical plate," Nonlinear Anal.: Modell. Control **14**(1), 73–84 (2009).

[20]S. Kamangar *et al.*, "Patient-specific 3D hemodynamics modelling of left coronary artery under hyperemic conditions," Med. Biol. Eng. Comput. **55**(8), 1451–1461 (2017).

[21]K. K. L. Wong, J. Wu, G. Liu, W. Huang, and D. N. Ghista, "Coronary arteries hemodynamics: Effect of arterial geometry on hemodynamic parameters causing atherosclerosis," Med. Biol. Eng. Comput. **58**(8), 1831–1843 (2020).

[22]S. H. Rambhia *et al.*, "Microcalcifications increase coronary vulnerable plaque rupture potential: A patient-based micro-CT fluid-structure interaction study," Ann. Biomed. Eng. **40**(7), 1443–1454 (2012).

[23]D. B. X. Liang, M. Xenos, Y. Alemu, S. H. Rambhia, I. Lavi, R. Kornowski, L. Gruberg, and S. Einav, "Biomechanical factors in coronary vulnerable plaques risk of rupture: Intravascular ultrasound-based patient specific fluid structure interaction studies," Coron. Artery Dis. **24**(2), 75–87 (2013).

[24]I. Abbas, "Natural frequencies of a poroelastic hollow cylinder," Acta Mech. **186**(1–4), 229–237 (2006).

[25]C. Shi *et al.*, "A study of noninvasive fractional flow reserve derived from a simplified method based on coronary computed tomography angiography in suspected coronary artery disease," Biomed. Eng. Online **16**(1), 1–15 (2017).

[26]H. Takagi *et al.*, "Optimized interpretation of fractional flow reserve derived from computed tomography: Comparison of three interpretation methods," J. Cardiovasc. Comput. Tomogr. **13**(2), 134 (2019).

[27]L. Zhong, J. M. Zhang, B. Su, R. S. Tan, J. C. Allen, and G. S. Kassab, "Application of patient-specific computational fluid dynamics in coronary and intra-cardiac flow simulations: Challenges and opportunities," Front. Physiol. **9**, 742 (2018).

[28]F. A. Alwawi, H. T. Alkasasbeh, A. M. Rashad, and R. Idris, "A numerical approach for the heat transfer flow of carboxymethyl cellulose-water based Casson nanofluid from a solid sphere generated by mixed convection under the influence of Lorentz force," Mathematics **8**(7), 1094 (2020).

[29]N. B. Casson, N. Past, A. S. Hamarsheh, F. A. Alwawi, and H. T. Alkasasbeh, "Heat transfer improvement in MHD natural convection flow of graphite oxide/carbon," Processes **8**(11), 1444 (2020).

[30]K. E. Hoque, S. Sawall, M. A. Hoque, and M. S. Hossain, "Hemodynamic simulations to identify irregularities in coronary artery models," J. Adv. Math. Comput. Sci. **28**(5), 1–19 (2018).

[31]I. E. Vignon-Clementel, C. Alberto Figueroa, K. E. Jansen, and C. A. Taylor, "Outflow boundary conditions for three-dimensional finite element modeling of blood flow and pressure in arteries," Comput. Methods Appl. Mech. Eng. **195**(29–32), 3776–3796 (2006).

[32]P. Eslami *et al.*, "Effect of wall elasticity on hemodynamics and wall shear stress in patient-specific simulations in the coronary arteries," J. Biomech. Eng. **142**(2), 0245031 (2020).

[33]F. Gijsen *et al.*, "Expert recommendations on the assessment of wall shear stress in human coronary arteries: Existing methodologies, technical considerations, and clinical applications," Eur. Heart J. **40**(41), 3421–3433 (2019).

[34]J. B. Park *et al.*, "Computational fluid dynamic measures of wall shear stress are related to coronary lesion characteristics," Heart **102**(20), 1655–1661 (2016).

[35]M. Zuin, G. Rigatelli, D. Vassilev, F. Ronco, A. Rigatelli, and L. Roncon, "Computational fluid dynamic-derived wall shear stress of non-significant left main bifurcation disease may predict acute vessel thrombosis at 3-year follow-up," Heart Vessels **35**, 297 (2020).

[36]A. M. Islam, A. Mohibullah, and T. Paul, "Cardiovascular disease in Bangladesh: A review," Bangladesh Hear. J. **31**(2), 80–99 (2017).

[37]A. Updegrove, N. M. Wilson, J. Merkow, H. Lan, A. L. Marsden, and S. C. Shadden, "SimVascular: An open source pipeline for cardiovascular simulation," Ann. Biomed. Eng. **45**(3), 525–541 (2017).

[38]J. Ahrens, B. Geveci, and C. Law, "ParaView: An end-user tool for large-data visualization," in *Visualization Handbook* (Elsevier, 2005), Vol. 836, pp. 717–731.

[39]T. Lundh, G. Y. Suh, P. DiGiacomo, and C. Cheng, "A Lagrangian cylindrical coordinate system for characterizing dynamic surface geometry of tubular anatomic structures," Med. Biol. Eng. Comput. **56**(9), 1659–1668 (2018).

[40]M. Gottsauner-Wolf, H. Sochor, D. Moertl, M. Gwechenberger, F. Stockenhuber, and P. Probst, "Assessing coronary stenosis. Quantitative coronary angiography versus visual estimation from cine-film or pharmacological stress perfusion images," Eur. Heart J. **17**(8), 1167–1174 (1996).

[41]B. F. Waller, "The eccentric coronary atherosclerotic plaque: Morphologic observations and clinical relevance," Clin. Cardiol. **12**(1), 14–20 (1989).

[42]T. Saeed, I. Abbas, and M. Marin, "A GL model on thermo-elastic interaction in a poroelastic material using finite element method," Symmetry (Basel) **12**(3), 488 (2020).

[43]R. Kumar and I. A. Abbas, "Deformation due to thermal source in micropolar thermoelastic media with thermal and conductive temperatures," J. Comput. Theor. Nanosci. **10**(9), 2241–2247 (2013).
[44]R. A and M. X. S. Malatos, "Advances in low-dimensional mathematical modeling of the human cardiovascular system," J. Hypertens. Manage. **2**(2), 17 (2016).
[45]M. M. S. Malatos, A. Raptis, M. A. Xenos, G. Kouvelos, A. Giannoukas, and E. L. Verhoeven, "A multiscale model for hemodynamic properties' prediction after fenestrated endovascular aneurysm repair. A pilot study," Hell. Vasc. J. **1**(2), 73–79 (2019).
[46]I. A. Abbas and M. Marin, "Analytical solution of thermoelastic interaction in a half-space by pulsed laser heating," Phys. E **87**, 254–260 (2017).
[47]T. Du, D. Hu, and D. Cai, "Outflow boundary conditions for blood flow in arterial trees," PLoS One **10**(5), e0128597 (2015).
[48]B. M. Johnston, P. R. Johnston, S. Corney, and D. Kilpatrick, "Non-Newtonian blood flow in human right coronary arteries: Steady state simulations," J. Biomech. **37**(5), 709–720 (2004).
[49]H. J. Kim, I. E. Vignon-Clementel, J. S. Coogan, C. A. Figueroa, K. E. Jansen, and C. A. Taylor, "Patient-specific modeling of blood flow and pressure in human coronary arteries," Ann. Biomed. Eng. **38**(10), 3195–3209 (2010).
[50]Y. Yoshikawa, M. Nakamoto, M. Nakamura, T. Hoshi, and E. Yamamoto, "On–site evaluation of CT–based fractional flow reserve using simple boundary conditions for computational fluid dynamics," Int. J. Cardiovasc. Imaging **36**, 337 (2019).
[51]D. N. Ku, "Blood flow in arteries," Annu. Rev. Fluid Mech. **29**(1), 399–434 (1997).
[52]P. D. Morris, J. Iqbal, C. Chiastra, W. Wu, F. Migliavacca, and J. P. Gunn, "Simultaneous kissing stents to treat unprotected left main stem coronary artery bifurcation disease; stent expansion, vessel injury, hemodynamics, tissue healing, restenosis, and repeat revascularization," Catheter. Cardiovasc. Interventions **92**, 1–12 (2018).
[53]H. Wang, T. Krüger, and F. Varnik, "Effects of size and elasticity on the relation between flow velocity and wall shear stress in side-wall aneurysms: A lattice Boltzmann-based computer simulation study," PLoS One **15**(1), e0227770 (2020).
[54]M. Ferrari, G. S. Werner, P. Bahrmann, B. M. Richartz, and H. R. Figulla, "Turbulent flow as a cause for underestimating coronary flow reserve measured by Doppler guide wire," Cardiovasc. Ultrasound **4**, 1–9 (2006).
[55]J. Liu, Y. Xiao, L. Zhang, M. Li, J. Tao, and S. Xu, "Extension at the downstream end of turbulent band in channel flow," Phys. Fluids **32**(12), 121703 (2020).
[56]B. C. Konala, A. Das, and R. K. Banerjee, "Influence of arterial wall-stenosis compliance on the coronary diagnostic parameters," J. Biomech. **44**(5), 842–847 (2011).
[57]S. Kamangar *et al.*, "Effect of stenosis on hemodynamics in left coronary artery based on patient-specific CT scan," Biomed. Mater. Eng. **30**(4), 463–473 (2019).